In: Advances in Chemistry Research. Volume 30
Editor: James C. Taylor
ISBN: 978-1-63484-183-2

Chapter 7

SEPARATED XRD ANALYSIS AND NON-LINEAR OPTICS FOR INTERACTION IN COMPOSITE MATERIALS OF CHIRAL CYANIDE BIMETALLIC COMPLEXES AND $LiMnO_2$ METAL OXIDE

Kohei Atsumi[1], Takashiro Akitsu[1,*], Pedro Sidónio Pereira Silva[2] and Vitor Hugo Nunes Rodrigues[2]

[1]Department of Chemistry, Faculty of Science,
Tokyo University of Science, Shinjuku-ku, Tokyo, Japan
[2]CEMDRX Physics Department,
University of Coimbra, Coimbra, Portugal

ABSTRACT

Chiral bimetallic complexes, $[CuL_2][M(CN)_2]_2$ (L = (*1R,2R*)-(+)-diphenylethylenediamine; M = Ag (CuAg) and Au (CuAu)) have been prepared and characterized by means of IR (infrared) spectra, magnetic susceptibility, and variable-temperature X-ray crystallography as single crystals or powder PXRD (powder X-ray diffraction). Both CuAg and CuAu crystallized in monoclinic space group *C*2. The thermally-accessible strain of the *b*-axis at 100-300 K is almost along the Jahn-Teller distortion. As composite materials (complexes: $LiMnO_2$ = 10:0, 9:1, 8:2, 7:3, 6:4, 5:5, 4:6, 3:7, 2:8, 1:9, 0:10) of typical layered-structure metal oxide $LiMnO_2$ (space group *Pmnm*) and CuAg or CuAu, interaction at the surface as well as crystalline states resulted in IR shift of Mn-O peaks, decreasing of ferromagnetism of $LiMnO_2$. Rietveld analysis of both components was carried out from separated PXRD patterns. For NLO (non-linear optics) inactive CuAu and $LiMnO_2$, composite materials of them exhibited second-harmonic generation efficiency due to grain interaction induced NLO for the first time.

INTRODUCTION

In recent years, social needs for rechargeable battery such as lithium or sodium ion batteries are increasing [1-5]. However, it is stated that a regular pattern of crystal structures distort due to effects from charge-discharge and prevent diffusion of ions in solid-state. Especially, developing a sodium ion battery requires large pores more than those for lithium ion battery known and rigidity of crystalline lattice against repeated redox reactions [6]. For improvement plan we made an approach to control the distortion of crystal structure. To control the distortion, we mixed chiral complex to metal oxide such as $LiMnO_2$ in order to grant anisotropy to metal oxide. We thought that by granting anisotropy to metal oxide, the distortion of metal oxide could be controlled to the less effective diffusion of ions.

For chiral complexes, a Cu(II) complex was employed since it exhibits local pseudo Jahn-Teller distortion. To date, we have been studying on a Cu(II) complex for decade. For example, thermally accessible lattice strain and local pseudo-Jahn-Teller distortion of Cu(II)–Ni(II) have been reported [7]. While Cu(II)–Co(III) crystallizes in the monoclinic (chiral and polar) space group $P2_1$ with $Z = 2$. The asymmetric unit of Cu(II)–Ni(II) contains tetranuclear cationic and mononuclear anionic moieties. An additional counter anion is also present, forming a two-dimensional layered structure of hydrogen bonds in the crystal. However, the ratios of (positive) lattice thermal expansion from 100 to 296 K are remarkable in the shortest axis (the *a*-axis) of Cu(II)–Co(III) (1.64%, 0.78%, and 0.30% for the *a*, *b*, and *c*-axes, respectively) as whole crystal structure. According to the *T* values [8], remarkable thermally accessible structural expansion is found along the axial Cu–O bonds.

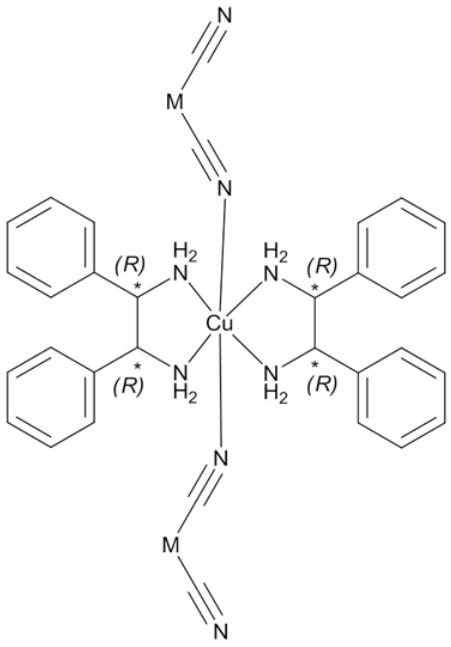

Figure 1. Chemical structures of CuM (M = Au, Ag).

Next, from the PXRD patterns of composite materials, we analyzed lattice constants, volumes, and fractional coordinates of $LiMnO_2$ for *Cu*, *cyGdCu*, and *Gd-Ni* [9] using Rietveld

method after separation of information of each component. When Rietveld method was carried out, we changed the θ cut values, to match the quantitative value of $LiMnO_2$ with the ratio we had prepared in order to decrease the effect from overlapping of neighborhood peaks. Layered crystal structure of $LiMnO_2$, a typical electrode material for lithium ion battery, is known to be *Pmnm*, a = 2.807, b = 5.756 and c = 4.557 Å [10], in which layers possessing Li^+ ions are stacked along the *b*-axis in other words (010) direction. The (002) planes stacked perpendicular to the c axis direction, while the (011) planes crossed the *a* and *b*-axes between the layers.

Finally, large non-linear optical properties were recently reported for L-alaninium perrhenate ($[C_3H_8NO_2]^+[ReO_4]^-$) [11]. Nonlinear optical materials may be applied in solar photovoltaic devices for wavelength conversion, which is necessary for the effective absorption of long-wavelength light such as NIR region [12-17].

In this context, herein, we have prepared and measured composite materials with complex side $[CuL_2][M(CN)_2]_2$ (CuM, M = Au, Ag) (Figure 1) and $LiMnO_2$ metal oxide (Figure 2).

1. Forming composite materials with the molar ratios of complexes: $LiMnO_2$ = 0:10 (pure metal complexes), 1:9, 2:8, 3:7,4:6, 5:5, 6:4, 7:3, 2:8, 1:9, 10:0 (pure $LiMnO_2$). Adsorption complexes to $LiMnO_2$ are confirmed by the shift of specific IR bands of $LiMnO_2$.
2. Observing the anisotropic lattice distortion of complexes or $LiMnO_2$ affected from $LiMnO_2$ or chiral complexes, and which plane indices shows structural anisotropy. Also the fractional coordinates of $LiMnO_2$ was calculated using Rietveld method.
3. Measuring the temperature dependence of crystal structures, magnetic properties, and NLO properties to elucidate structures of composite materials.

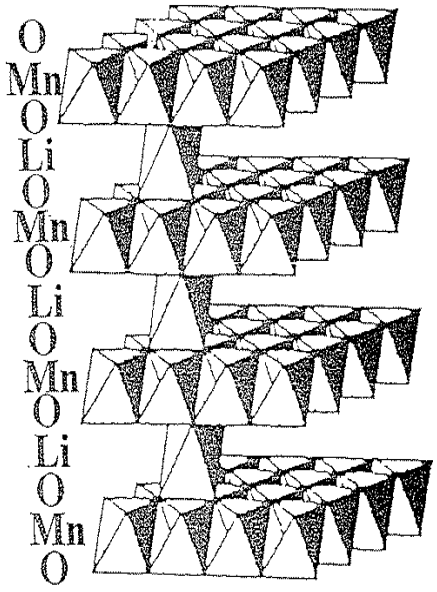

Figure 2. Schematic layered structure of $LiMnO_2$.

EXPERIMENTAL SECTION

Preparations

The CuAu bimetallic assembly was obtained by the slow diffusion of a DMSO solution (5 mL) of $[CuL_2](NO_3)_2$ (0.0244 g, 0.04 mmol) in an aqueous solution (45 mL) of $K[Au(CN)_2]$ (0.0461 g, 0.016 mmol) at 293 K. After several days, purple prismatic single crystals were obtained from the surface of the solution. Yield: 0.0108 g (59.1%). Anal. Calcd. for $C_{32}H_{32}N_8Ag_2Cu$: C, 38.97; H, 3.27; N, 11.36. Found: C, 39.05; H, 3.03; N, 11.30%. Infrared spectra (IR) (KBr, cm^{-1}): 413 (m), 503 (w), 568 (m), 627 (w), 698 (s), 762 (s), 856 (w), 913 (w), 952 (w), 963 (w), 1016 (s), 1074 (w), 1133 (w), 1198 (w), 1275 (w), 1313 (w), 1375 (w), 1455 (m), 1498 (m), 1589 (m), 2113(s) (C≡N), 3030 (w), 3069 (w), 3138 (m), 3236 (m), 3320 (m), and 3438 (m).

The CuAg bimetallic assembly was obtained by using $K[Ag(CN)_2]$ (0.0244 g, 0.16 mmol) instead of $K[Au(CN)_2]$. Yield: 0.0233 g (33.4%). Anal. Calcd. for $C_{32}H_{32}N_8Ag_2Cu$: C, 47.57; H, 3.99; N, 13.87. Found: C, 47.27; H, 3.85; N, 13.81%. IR (KBr, cm^{-1}): 414 (m), 485 (w), 560 (w), 574 (m), 627 (m), 700 (s), 765 (s), 827 (w), 854 (w), 917 (w), 954 (m), 1016 (s), 1076 (w), 1128 (m), 1230 (w), 1267 (w), 1315 (w), 1383 (w), 1455 (s), 1497 (w), 1585 (s), 1629 (w), 2116 (s) (C≡N), 2916 (w), 3029 (w), 3063 (w), 3139 (m), 3233 (m), 3311 (m), and 3435 (m).

Composite materials of metal complexes and $LiMnO_2$ were prepared by mixing with grinding in the solid states by the molar ratios of complex: $LiMnO_2$ = 10:0, 9:1, 8:2, 7:3, 6:4, 5:5, 4:6, 3:7, 2:8, 1:9, 10:0.

Physical Measurements

Infrared spectra (IR) were recorded as KBr pellets on a JASCO FT-IR 4200 Plus spectrophotometer at 298 K. Powder XRD patterns were measured by with a RIGAKU RINT 2500 diffractometer with CuKα radiation (λ = 1.54184 Å) and Rigaku SmartLab at The University of Tokyo with CuKα radiation. Lattice constants were evaluated by a Rietveld method. Elemental analyses (C, H, and N) were performed with a Perkin-Elmer 2400II CHNS/O analyzer at Tokyo University of Science. The magnetic properties were investigated using a Quantum Design MPMS-XL (superconducting quantum interference device magnetometer) at an applied field of 1.0 T in the temperature range of 5-300 K. Powder samples were measured in a pharmaceutical cellulose capsule.

X-Ray Crystallography of Single Crystals

Single crystals were glued on top of a glass fiber and coated with a thin layer of epoxy resin to measure the diffraction data. Intensity data were collected on a Bruker APEX2 CCD diffractometer with graphite monochromated MoKα radiation (λ = 0.71073 Å). Data analysis was carried out using the SAINT program package. The structures were solved by direct methods with SHELXS-97 [18], expanded by Fourier techniques, and refined by full-matrix

least-squares methods based on F^2 with the program SHELXL-97 [18]. An empirical absorption correction was applied in the program SADABS. All non-hydrogen atoms were readily located and refined by anisotropic thermal parameters. All hydrogen atoms were located at geometrically calculated positions and refined using riding models.

Non-Linear Optical Measurements

The Second-Harmonic Generation (SHG) efficiencies were measured using the Kurtz and Perry powder method [19]. The measurements were performed at a wavelength of 1064 nm produced by a Nd:YAG laser, which operated at 10 Hz and produced 10-ns pulses with a pulse energy of 11 mJ. The sample preparation procedure was as follows: the material was milled to a fine powder, compacted in a mount, and installed in the sample holder. Sample grain sizes were not standardized. In some cases, signals between individual measurements varied by as much as ± 10%. To allow a proper comparison with the urea reference material, the measurements were averaged over several laser thermal cycles.

RESULTS AND DISCUSSION

Structural description of single crystals. The crystallographic data and selected bond lengths for CuAu are listed in Tables 1 and 2, respectively. CuAu crystallizes in monoclinic, (chiral and polar) space group *C2* with $Z = 4$, and the asymmetric unit of CuAu ($[CuL_2][Au(CN)_2]_2$) (Figure 3).

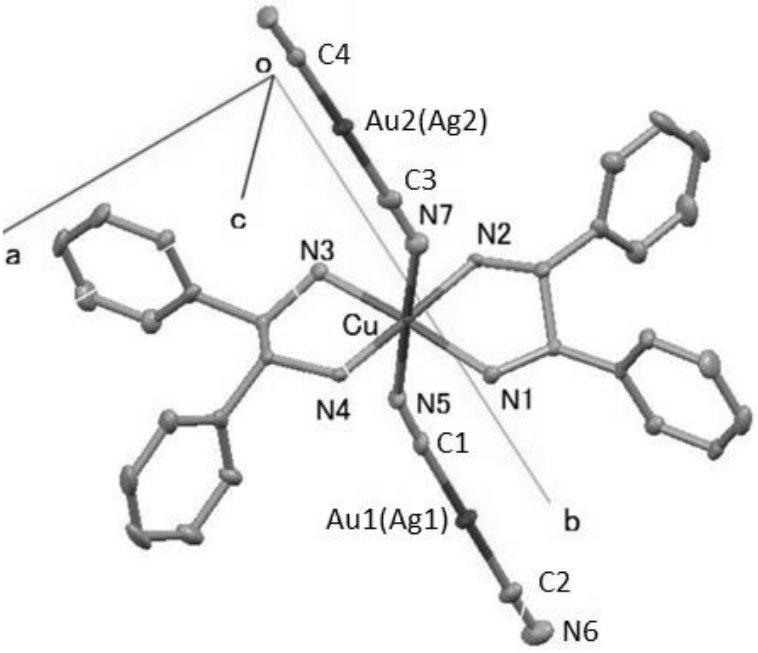

Figure 3. Structure of CuM (M = Au, Ag).

Table 1. Crystal and structure refinement data for CuAu

Temperature	100 K	200 K	300 K
	CCDC = 1412710	CCDC = 1412711	CCDC = 1412712
Empirical formula	$C_{32}H_{32}N_8Au_2Cu$	$C_{32}H_{32}N_8Au_2Cu$	$C_{32}H_{32}N_8Au_2Cu$
Formula weight	986.13	986.13	986.13
Crystal system	Monoclinic	Monoclinic	Monoclinic
Space group	*C*2	*C*2	*C*2
a (Å)	27.418(4)	27.543(2)	27.668(2)
b (Å)	10.0379(4)	10.0195(2)	9.9859(2)
c (Å)	12.0499(15)	12.2204(9)	12.4144(9)
β (°)	98.409(9)	98.6220(10)	98.914(4)
V (Å^3)	3280.7(8)	3334.4(4)	3388.5(4)
Z	4	4	4
Crystal size (mm)	0.12 0.11 0.11	0.12 0.11 0.11	0.12 0.11 0.11
Density (calculated) (g/cm^{-3})	1.997	1.964	1.933
Absorption coefficient (mm^{-1})	9.599	9.444	9.293
F(000)	1868	1868	1868
θ range for data collection (°)	2.43 to 27.59	2.42 to 27.47	2.40 to 27.44
Limiting indices	-35< = *h*< = 33	-33< = *h*< = 35	-35< = *h*< = 33
	-6< = *k*< = 12	-6< = *k*< = 12	-6< = *k*< = 12
	-15< = *l*< = 15	-15< = *l*< = 15	-15< = *l*< = 16
Reflections collected	9078	9114	9287
Absorption correction	Empirical	Empirical	Empirical
Max. and min. transmission	0.2000 and 0.2000	0.3970 and 0.4231	0.4018 and 0.4280
Data/restraints/parameters	4896/1/389	4936/1/389	5019/1/388
Final *R* indices	R_1 = 0.0229	R_1 = 0.0235	R_1 = 0.0274
[*I*>2sigma(*I*)]	wR_2 = 0.0511	wR_2 = 0.0550	wR_2 = 0.0650
R indices (all data)	R_1 = 0.0234	R_1 = 0.0246	R_1 = 0.0306
	wR_2 = 0.0514	wR_2 = 0.0553	wR_2 = 0.0663
Goodness-of-fit on F^2	1.058	1.026	1.003
Flack parameter	0.006(8)	0.007(7)	0.014(8)
Largest diff. peak and hole	1.238 and-0.441 e.Å^{-3}	1.207 and-0.231 e.Å^{-3}	1.311 and-0.361 e.Å^{-3}

Table 2. Selected bond distance (Å) and T value of CuAu

	100 K	200 K	300 K
Cu－N1	2.040	2.043	2.050
Cu－N2	2.003	2.004	2.005
Cu－N3	2.060	2.057	2.037
Cu－N4	2.013	2.009	2.010
Cu－N5	2.430	2.446	2.453
Cu－N7	2.470	2.495	2.515
T	0.8282	0.8210	0.8153

The ratios of (positive) lattice thermal expansion from 100 K to 296 K are remarkable in the shortest axis (the *a*-axis) of CuAu (0.91%, -0.52%, and 3.02% for the *a*, *b*, *c*-axis, respectively; Table1). According to the index of tetragonal distortion, (T = Cu-$N_{in\text{-}plane}$/Cu-N_{axial}), and the ratios of bond lengths, the thermally-accessible structural changes are

attributed to the in-plane Cu-N bond length, and the direction of the *a*-axis and two axial Cu-N bonds (Cu-N5 and Cu-N7) are not parallel to each other. The *b*-axis direction exhibited negative thermal expansion. Consequently, some *T* values indicated remarkable thermally-accessible structural expansion (Table 2).

Table 3. Crystal and structure refinement data for CuAg

Temperature	100 K	200 K	300 K
	CCDC = 1412707	CCDC = 1412708	CCDC = 1412709
Empirical formula	$C_{32}H_{32}N_8Ag_2Cu$	$C_{32}H_{32}N_8Ag_2Cu$	$C_{32}H_{32}N_8Ag_2Cu$
Formula weight	805.93	805.93	805.93
Crystal system	Monoclinic	Monoclinic	Monoclinic
Space group	*C*2	*C*2	*C*2
a (Å)	27.325(3)	27.4201(19)	27.568(2)
b (Å)	10.2163(13)	10.1743(6)	9.9959(2)
c (Å)	11.8903(15)	12.0590(7)	12.2344 (9)
β (°)	98.404(2)	98.6790(10)	98.914(4)
V (Å^3)	3283.7(7)	3325.7(4)	3388.5(4)
Z	4	4	4
Crystal size (mm)	0.15 0.15 0.14	0.15 0.15 0.14	0.15 0.15 0.14
Density (calculated) (g/cm^{-3})	1.634	1.614	1.605
Absorption coefficient (mm^{-1})	1.857	1.834	1.830
F(000)	1612	1612	1612
θ range for data collection (°)	2.46 to 27.51	2.46 to 27.51	2.46 to 27.51
Limiting indices	-35< = *h*< = 23	-35< = *h*< = 23	-35< = *h*< = 23
	-12< = *k*< = 13	-12< = *k*< = 13	-12< = *k*< = 13
	-13< = *l*< = 15	-13< = *l*< = 15	-13< = *l*< = 15
Reflections collected	8755	8755	8755
Absorption correction	Empirical	Empirical	Empirical
Max. and min. transmission	0.764 and 0.771	0.764 and 0.771	0.764 and 0.771
Data/restraints/parameters	6764/1/388	6764/1/388	6764/1/388
Final *R* indices	R_1 = 0.0273	R_1 = 0.0328	R_1 = 0.0354
[*I*>2sigma(*I*)]	wR_2 = 0.0710	wR_2 = 0.0710	wR_2 = 0.0710
R indices (all data)	R_1 = 0.0288	R_1 = 0.0288	R_1 = 0.0288
	wR_2 = 0.0721	wR_2 = 0.0804	wR_2 = 0.0833
Goodness-of-fit on F^2	1.067	1.111	1.054
Flack parameter	0.010(7)	0.009(8)	0.004(7)
Largest diff. peak and hole	1.107 and-0.511 e.Å^{-3}	1.302 and-0.338 e.Å^{-3}	1.266 and-0.455 e.Å^{-3}

Table 4. Selected bond distance (Å) and T value of CuAg

	100 K	200 K	300 K
Cu－N1	2.059	2.031	2.023
Cu－N2	2.011	2.011	2.015
Cu－N3	2.045	2.051	2.065
Cu－N4	2.010	2.004	2.001
Cu－N5	2.426	2.424	2.440
Cu－N7	2.490	2.514	2.534
T	0.8264	0.8191	0.8146

The crystallographic data and selected bond lengths for CuAg are listed in Tables 3 and 4, respectively. Similar to CuAu, CuAg crystallizes in monoclinic, (chiral and polar) space

group *C2* with $Z = 4$. The asymmetric unit of CuAg ($[CuL_2][Ag(CN)_2]_2$) is also shown in Figure 3.

The ratios of (positive) lattice thermal expansion from 100 K to 296 K are remarkable in the shortest axis (the *a*-axis) of CuAg (0.89%, -2.16%, and 2.89% for the *a*, *b*, *c*-axes, respectively; Table 3). According to the index of tetragonal distortion, (T = Cu-$N_{in\text{-}plane}$/Cu-N_{axial}), and the ratios of bond lengths, the thermally-accessible structural changes are attributed to the in-plane Cu-N bond length, and the direction of the *c*-axis and two axial Cu-N bonds (Cu-N5 and Cu-N7) are not parallel to each other. The degree of thermally-accessible structural expansion of CuAg is larger than that of CuAu (Table 4).

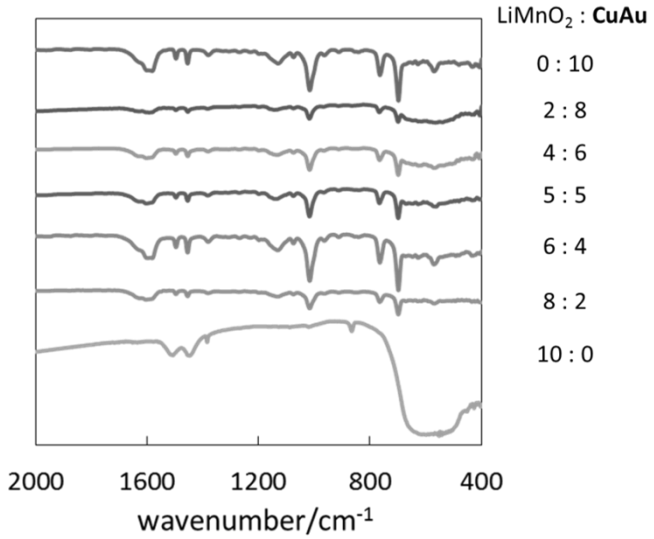

Figure 4. IR spectra of the CuAu and $LiMnO_2$ composite materials of various ratios at 298 K.

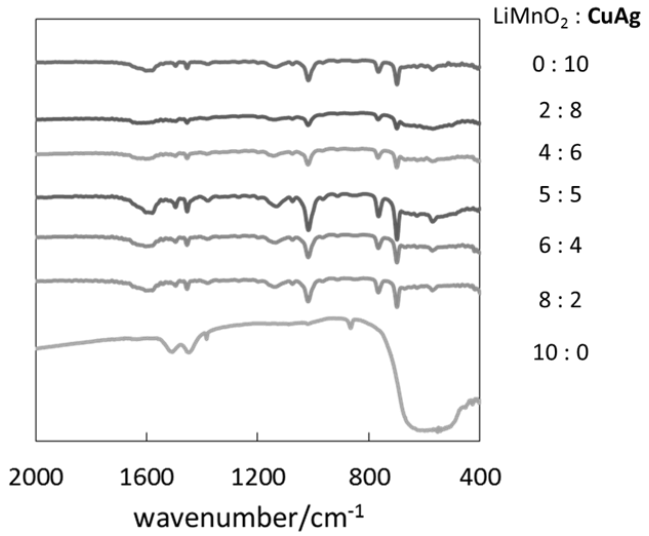

Figure 5. IR spectra of the CuAg and $LiMnO_2$ composite materials of various ratios at 298 K.

Preparations of composite materials. Figures 4 and 5 exhibit IR spectra of CuAu or CuAg and their composite materials with the molar ratios of complex: $LiMnO_2$ = 0:10 (pure complex), 1:9, 2:8, 3:7,4:6, 5:5, 6:4, 7:3, 2:8, 1:9, 10:0 (pure $LiMnO_2$). Low-wavenumber shifts of IR spectra of $LiMnO_2$ around 600 cm^{-1} (Mn-O) due to increasing in ratios of CuAu or CuAg was observed. The shift of CuAu and CuAg results from indicating adsorption of metal complexes to the surface of $LiMnO_2$.

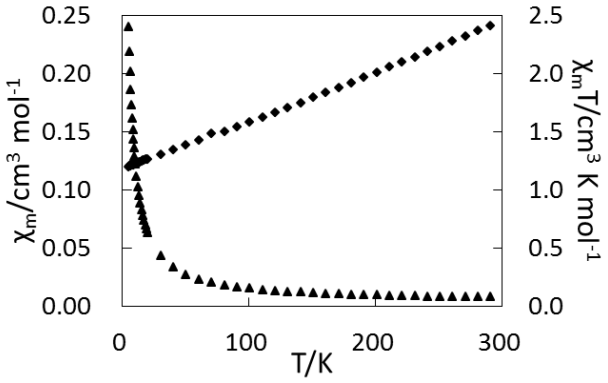

Figure 6. The χ m vs T and χ mT vs T plots for CuAu.

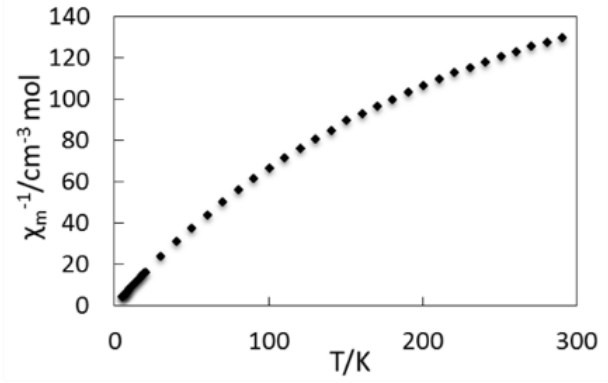

Figure 7. The χ^{-1} vs T plots for CuAu.

Magnetic properties. The $\chi_m T$ vs *T*, $\chi_m T$ vs *T* and χ^{-1} vs *T* plots for CuAu and CuAg in the range of 5-300 K were shown in Figures 6-9. The magnetic behavior and Weiss constants (θ = -0.4438 and -0.4201 K for CuAu and CuAg, respectively), of two samples derived from fitting with the Curie-Weiss equation are in good agreement with their crystal structure (i.e., decrease mononuclear Cu(II) complexes with *s* = ½). Both CuAu and CuAg have no hysteresis widths of ferromagnetism in H-M plots. As is often the case mononuclear Cu(II) complexes, weakly paramagnetic compound indicates relatively large effective magnetic moment at low-temperature region because of a certain experimental programs (relatively larger diamagnetic contribution).

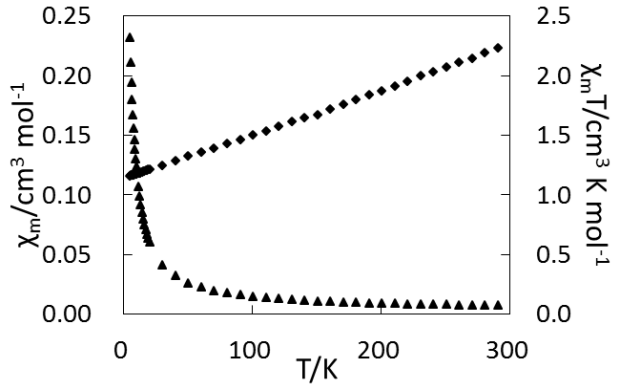

Figure 8. The χ_m vs T and $\chi_m T$ vs T plots for CuAg.

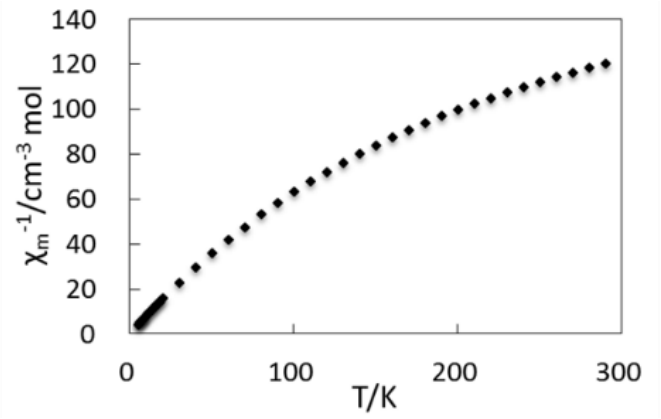

Figure 9. The χ^{-1} vs T plots for CuAg.

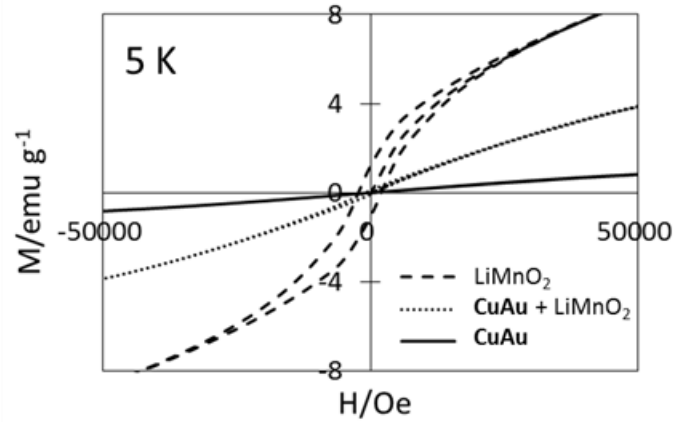

Figure 10. The hysteresis curves for CuAu, $LiMnO_2$ and composite materials.

Figures 10-13 exhibit magnetic data of complexes with the related materials, respectively.

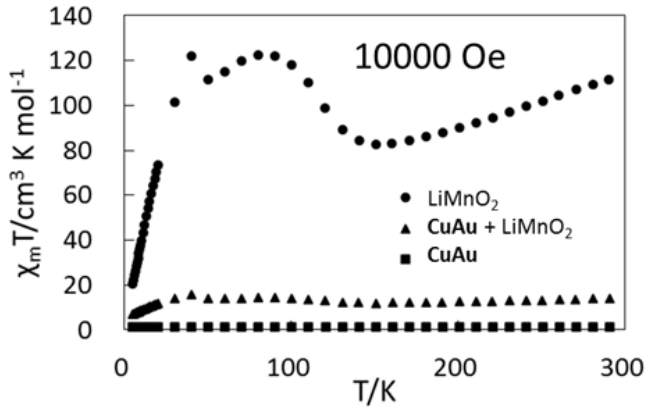

Figure 11. The χ mT vs T plots for CuAu, $LiMnO_2$ and composite materials.

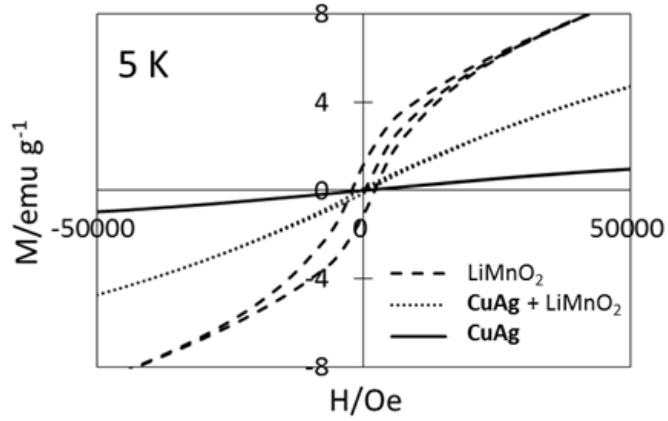

Figure 12. The hysteresis curves for CuAg, $LiMnO_2$ and composite materials.

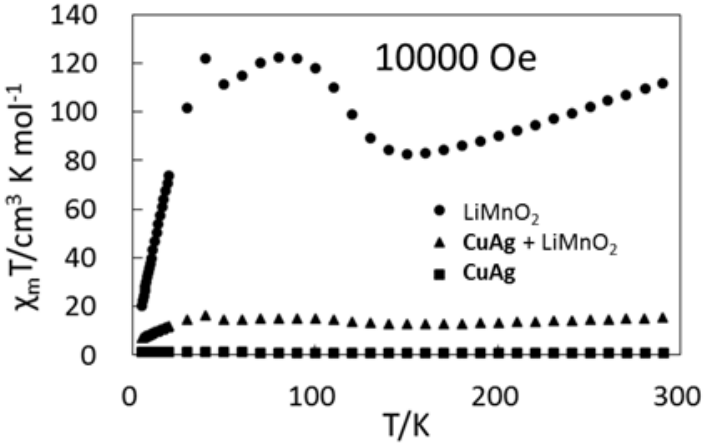

Figure 13. The χ mT vs T plots for CuAg, $LiMnO_2$ and composite materials.

Pure $LiMnO_2$ exhibited ferromagnetism as shown in both hysteresis curves of H-M plots (Figures10 and 12). While both complexes did not exhibit distinct character of ferromagnetism [20] under the same conditions. However, both 5:5 composite materials of complex and $LiMnO_2$ exhibited weak ferromagnetic character. Not only IR spectra but also magnetic data suggested interaction between complex and $LiMnO_2$ as the composite materials. In this way, ferromagnetism character of $LiMnO_2$ decreased because of adsorption of complexes.

PXRD patterns of various molar ratios. Figures 14 and 15 PXRD patterns of the composite materials of CuAu (Figure 14), or CuAg (Figure 15) and $LiMnO_2$. From the PXRD patterns of composite materials, we analyzed lattice constants and fractional coordinates of CuAu or CuAg using Rietveld method after separation of data of each component. When Rietveld analysis was carried out, we changed the θ cut values, to match the quantitative value of $LiMnO_2$ with the ratio we had prepared in order to decrease the effect from overlapping of neighborhood peaks.

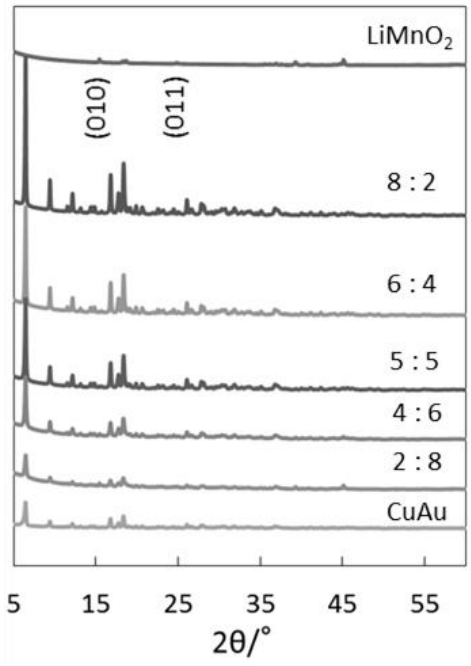

Figure 14. XRD patterns of the CuAu and $LiMnO_2$ composite materials of various ratios at 300 K.

Table 5 and 6 shows the lattice constants of CuAu and CuAg, respectively. Table 12 and 13 list x, y and z fractional coordinates of CuAu and CuAg atoms. Tables 7-8 show the lattice constants of $LiMnO_2$ of pure $LiMnO_2$, CuAu- $LiMnO_2$ and CuAg- $LiMnO_2$ composite materials, respectively. Tables 9-11 list x, y and z fractional coordinates of pure $LiMnO_2$, CuAu- $LiMnO_2$ and CuAg- $LiMnO_2$ composite materials, respectively. Increasing complex ratio in composite materials, lattice constant of *b*-axis of CuAu increased. In contrast, lattice constant of *b*-axis of CuAg decreased. Altough CuAu and CuAg has same structure (space group *C2*), each composite material with CuAu and CuAg rather than $LiMnO_2$ exhibited different anisotropy in the *b*-axis direction. It depends on soft crystal grains of complexes.

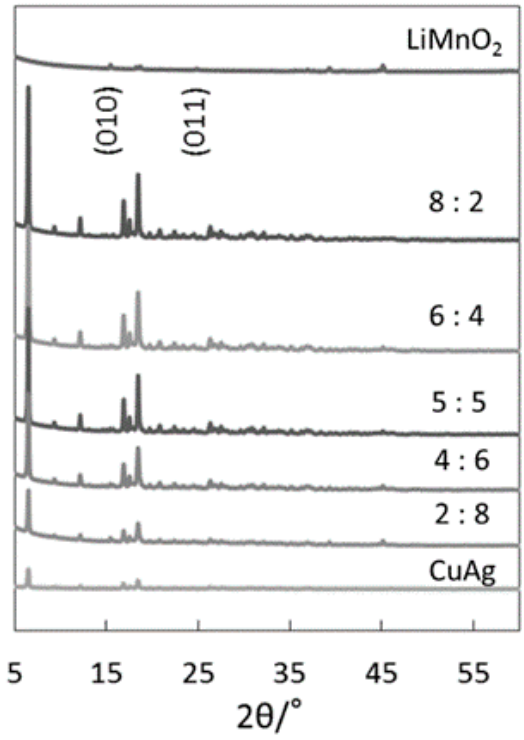

Figure 15. XRD patterns of the CuAg and $LiMnO_2$ composite materials of various ratios at 300 K.

Table 5. Lattice constants (*a*, *b*, and *c* axes, Å) of CuAu for the CuAu-$LiMnO_2$ composite materials

CuAu : $LiMnO_2$	*a*-axis	*b*-axis	*c*-axis
5 : 5	27.6629	9.9753	12.4515
10 : 0	27.6737	9.9799	12.0875

Table 6. Lattice constants (*a*, *b*, and *c* axes, Å) of CuAg for the CuAg-$LiMnO_2$ composite materials

CuAg : $LiMnO_2$	*a*-axis	*b*-axis	*c*-axis
5 : 5	27.5437	10.2981	11.9855
10 : 0	27.5428	10.1108	12.1228

Table 7. Lattice constants (*a*, *b*, and *c* axes, Å) of $LiMnO_2$ for the CuAu-$LiMnO_2$ composite materials

CuAu : $LiMnO_2$	*a*-axis	*b*-axis	*c*-axis
5 : 5	2.4494	5.7763	4.6008
0 : 10	2.8082	5.7435	4.5855

Table 8. Lattice constants (*a*, *b*, and *c* axes, Å) of $LiMnO_2$ for the CuAg-$LiMnO_2$ composite materials

CuAg : $LiMnO_2$	*a*-axis	*b*-axis	*c*-axis
5 : 5	2.8464	5.7391	4.585
0 : 10	2.8082	5.7435	4.5855

Table 9. Fractional coordinates for x, y and z (Å) for pure $LiMnO_2$.

	x	y	z
Mn1	0.25	0.624397	0.25
Li1	0.25	0.123789	0.25
O1	0.25	0.115222	0.25
O2	0.25	0.629828	0.25

Table 10. Fractional coordinates for x, y and z (Å) of $LiMnO_2$ atoms for the 5 : 5 CuAu-$LiMnO_2$ composite materials

	x	y	z
Mn1	0.25	0.6347	0.25
Li1	0.25	0.126	0.25
O1	0.25	0.144	0.75
O2	0.25	0.602	0.75

Table 11. Fractional coordinates for x, y and z (Å) of $LiMnO_2$ atoms for the 5: 5 CuAg-$LiMnO_2$ composite materials

	x	y	z
Mn1	0.25	0.6347	0.25
Li1	0.25	0.126	0.25
O1	0.25	0.144	0.75
O2	0.25	0.602	0.75

Non-linear optical measurements. To determine the non-linear optical responses of the complexes and composite materials, the authors measured the SHG (second harmonic generation) efficiency using the Kurtz-Perry method [21] with polycrystalline samples.

CuAu and CuAg exhibited SHG signals of 0 and 0.05 times that of the urea standard (with an error of less than 10%), while CuAu or CuAg (space group C*2*) exhibited signals, 5:5 composite materials of CuAu or CuAg and $LiMnO_2$ exhibited SHG signals of 0.07 and 0.12 times, while $LiMnO_2$ (space group P*mnm*) exhibited no signals. It should be noted that achiral $LiMnO_2$ induced structural strain of chiral CuAu indicating no NLO signals to indicate weak SHG by forming composite materials of crystal grains.

Table 12. Fractional coordinates for x, y and z (Å) of CuAu atoms for the CuAu-$LiMnO_2$ composite materials

CuAu : $LiMnO_2$	5 : 5			10 : 0		
	x	y	z	x	y	z
Cu	0.4953	0.5073	0.2499	0.5059	0.5079	0.2237
Au1	0.4440	0.06829	0.4659	0.4411	0.06829	0.4638
Au2	0.5550	0.9325	0.05620	0.5542	0.9344	0.05141
N1	0.4390	0.4725	0.1237	0.9677	0.1809	-0.7370
N2	0.5507	0.4804	0.3922	1.081	1.751	0.9450
N3	0.5583	1.214	-0.02126	0.5321	-0.3673	-0.3725
N4	0.4651	0.6853	0.3067	0.9537	1.732	0.3859
N5	0.4504	0.3245	0.3780	0.5173	0.9048	0.1211
N6	0.5529	0.6116	0.1349	0.3487	0.4909	1.060
N7	0.5319	0.3205	0.2305	0.1546	1.495	-0.2634
N8	0.4466	-0.1990	0.5793	-0.07158	-0.3741	3.044
C1	0.7042	0.4260	0.5547	0.6500	-2.561	0.4395
C2	0.6729	0.3859	0.4986	0.2403	0.9382	-0.4075
C3	0.7045	0.5625	0.4323	1.272	1.5217	0.5699
C4	0.5711	1.124	0.08271	0.5767	1.120	-2.011

Table 13. Fractional coordinates for x, y and z (Å) of CuAg atoms for the CuAg-$LiMnO_2$ composite materials

CuAg : $LiMnO_2$	50			100		
	x	y	z	x	y	z
Cu	0.5015	0.2183	0.2504	0.5016	0.3230	0.1846
Ag1	0.4441	-0.2181	0.4415	0.4354	-0.2181	0.3756
Ag2	0.5562	0.6560	0.04770	0.5688	0.6485	0.1280
N1	0.4640	0.3775	0.2973	0.5065	0.4027	0.3992
N2	0.5364	0.05380	0.2973	0.5252	0.2457	0.4633
N3	0.4469	0.2165	0.1171	0.5783	0.4994	-0.3209
N4	0.5604	0.2282	0.3724	0.3544	-0.04909	0.6861
N5	0.5475	0.3598	0.1313	0.3544	0.3728	-0.1009
N6	0.4556	0.07830	0.3621	0.3139	0.1432	0.4191
N7	0.4372	-0.4990	0.5574	0.3674	-0.1417	0.8007
N8	0.5622	0.9340	-0.07350	0.6170	0.7583	-0.2039
C1	0.3601	0.7072	0.2333	0.6016	0.2483	-0.2728
C2	03092	0.5739	0.3366	0.3702	0.6519	0.3043
C3	0.3196	0.6939	0.2925	0.4480	0.6760	0.09809
C4	0.7002	0.07790	0.5815	0.7074	0.2429	0.3673

CONCLUSION

We synthesized new chiral bimetallic assemblies (CuAu and CuAg) and solved their single crystal structures at 100, 200 and 300 K. In the *a* and *c*-axes, the ratios of positive thermal expansion of lattice from 100 K to 300 K are remarkable, while in the *b*-axis,

negative thermal expansion are remarkable. We had investigated the effect of composite between chiral complex and $LiMnO_2$. By changing the complexes to adsorb, variation had been observed in magnetic properties and IR spectra. From the view of magnetic properties, $LiMnO_2$ exhibited decreasing of ferromagnetism by combined with CuAu or CuAg that has paramagnetism. Using Rietveld method, lattice constants of the composite materials exhibited different anisotropy in the *b*-axis direction remarkably. From the view of NLO, however, CuAu exhibited increasing of NLO by combined with $LiMnO_2$ having no SHG though pure CuAu indicates no SHG.

SUPPLEMENTAL DATA

CCDC 1412707-1412712 contain the supplementary crystallographic data. These data can be obtained free of charge via http: //www.ccdc.cam.ac.uk/conts/retrieving.html, or from the Cambridge Crystallographic Data Centre, 12 Union Road, Cambridge CB2 1EZ, UK; fax: (+ 44) 1223-336-033; or E-mail: deposit@ccdc.cam.ac.uk. Magnetic data are also deposited.

REFERENCES

[1] Yao, M., Senoh, H., Sakai, T., Kiyobayashi, T., *Int, J. Electrochem. Sci*., 2011, 6, 2905.
[2] Yao, M., Senoh, H., Yamazaki, S., Shiroma, Z., Sakai, T., Yamada, K., *J. Power Sources*, 2010, 195, 8336.
[3] Yao, M., Araki, M., Senoh, H., Yamazaki, S., Sakai, T., Yasuda, K., *Chem. Lett*., 2010, 39, 950.
[4] Yao, M., Senoh, H., Sakai, T., kiyobayashi, T., *J. Power Sources*, 2012, 202, 364.
[5] Dbart, A., Paterson, Allan. J., Bao, J., Bruce, P. G., *Angrew. Chem. Int. Ed*., 2008, 47, 4521.
[6] Wenzel, S., Hara, T., Janek, J., Adelhelm, P., *Energy Environ. Sci*., 2011, 4, 3342.
[7] Akitsu, T., Endo, Y., Okawara, M., Kimoto, Y., Ohwa, M., *Open Cryst. J*., 2011, 4, 2.
[8] Hathaway, B. J., Billing, D. E., *Coord. Chem. Rev.*, 1970, 5, 143.
[9] Orii, Y., Atsumi, K., Matsuno, M., Machida, Y., Akitsu, *Adv. in Chem. Res.*, 26, Nova Science Publishers, Inc. (NY, USA), in press.
[10] Tu, X. Y., Shu, K. Y., *J. Solid State Electrochem.*, 2008, 12, 245.
[11] Rodrigues, V. D., Costa, M. M. R. R., Gomes, E. M., Isakov, D., Belsley, M. S., *Cent. Eur. J. Chem*., 2014, 12, 1016.
[12] Rong, J. W., Senior, M. I., Wen, H. W., Chung, Y. L., *IEEE*, 2008, 55, 240.
[13] Rong, J. W., Senior, M. I., Wen, H. W., *IEEE*, 2008, 55, 953.
[14] Tarun K. B, Joon I. J, Jung H. S, Christos D. M, Arthur J. F, John B. K, and Mercouri G. K, *J. Am. Chem. Soc.*, 2010, 132, 3484.
[15] Zhisheng, Z. F., Tian, X. D., Quan, L., Qianqian, W., Hui, W., Xin, Z., Bo, X., Dongli, Y., Julong, H., Hui, T. W., Yanming, M., Yongjun, T., *J. Am. Chem. Soc.*, 2012, 134, 12362.
[16] Sebastian, B., Ullrich, S., John, M. L., *J. Am. Chem. Soc*., 2012, 134, 1946.
[17] Humbury, G. A., Borovkov, V. V., Inoue, Y., *Chem. Soc. Rev.*, 2008, 108, 1.

[18] Sheldrick, G., *Acta Cryst., A*, 2008, 64, 122.
[19] Kurtz, S. K., Perry, T. T., *J. Appl. Phys*., 1968, 39, 3798.
[20] Kobayashi, M., Akitsu, T., *J. Chem. Chem. Eng.*, 2014, 8, 557.